Interference effects with surface plasmons

Kuzmin, N.V.

Chapter 5

Phase factors in light-plasmon scattering

We present an experimental study of the scattering of surface plasmons that propagate along a smooth metallo-dielectric interface off sub-wavelength slits milled in a metal film. We use configurations containing a combination of two and three slits to obtain detailed information on the scattering phase, and the tunneling amplitude and phase. We also demonstrate that the light transmitted by our structures has a space-variant polarization.

5.1 Introduction

When light impinges on the interface between a dielectric, characterized by a (real) dielectric coefficient $\epsilon_{\mathrm{d}}(\omega)$, and a metal surface with dielectric coefficient $\epsilon_{\mathrm{m}}(\omega)$, and that interface is not perfectly smooth, part of the light will be reflected, part will be directly scattered into free-space modes, and part will be converted into surface modes [8,24]. For almost all metals these surface modes are heavily damped. However, on gold, silver and aluminium, the surface mode is only weakly damped (in certain wavelength ranges) and is known as the surface plasmon or, more precisely, as the surface plasmon polariton [8,93,94]. This mode appears when the real parts of the dielectric coefficients of the metal and of the dielectric, $\epsilon'_{\mathrm{m}}(\omega)$ and $\epsilon_{\mathrm{d}}(\omega)$, have opposite sign. In essence, this means that $\epsilon'_{\mathrm{m}}(\omega) < 0$. Since $\epsilon'_{\mathrm{m}}(\omega) = n^2(\omega) - \kappa^2(\omega)$, with $n(\omega)$ and $\kappa(\omega)$ the real and imaginary parts of the refractive index, the requirements reads $n(\omega) < \kappa(\omega)$ or, in order to have a low-loss surface plasmon, $n(\omega) \ll \kappa(\omega)$. In the near-infrared spectral region silver and gold fulfill these requirements and are the metals of choice for the study of surface plasmons.

For a planar metallo-dielectric interface that supports a surface plasmon one can write for the wave vector of that mode [8]:

$$k_{\mathrm{sp}} = \frac{\omega}{c}\sqrt{\frac{\epsilon_{\mathrm{d}}\epsilon_{\mathrm{m}}}{\epsilon_{\mathrm{d}} + \epsilon_{\mathrm{m}}}}. \tag{5.1}$$

Since ϵ_{m} is complex, so is k_{sp}. In the present chapter the imaginary part of k_{sp}, which quantifies the damping of the surface plasmon, plays only a minor role and will be largely neglected. The real part of k_{sp} yields the propagation constant of the surface plasmon; it can be calculated by replacing ϵ_{m} in Eq. (5.1) by its real part ϵ'_{m} [8]. Henceforth, we will denote the propagation constant as k_{sp}.

Since $\epsilon_{\mathrm{d}} > 0$ and $\epsilon'_{\mathrm{m}} < 0$, we have $k_{\mathrm{sp}} - \sqrt{\epsilon_{\mathrm{d}}}\omega/c > 0$, showing that there is a mismatch between the wave vectors of the interface-bound surface plasmon and of the unbound modes at the same frequency. Because of this mismatch surface plasmons can not be excited on a smooth metallo-dielectric interface when it is illuminated by a plane wave. However, a prism coupler [25, 26] or a corrugation of the interface will be able to supply the missing momentum so that the incident light will couple to surface plasmons. By the same token, surface plasmons are able to couple to free-space radiation wherever the interface is not smooth. So, whenever a surface plasmon traveling along a smooth metallo-dielectric interface encounters a bump, trench, hole or slit, it is scattered into a transmitted plasmon, a reflected plasmon, and into free-space radiation (see Fig. 4.1b in Chapter 4). Associated with each of these

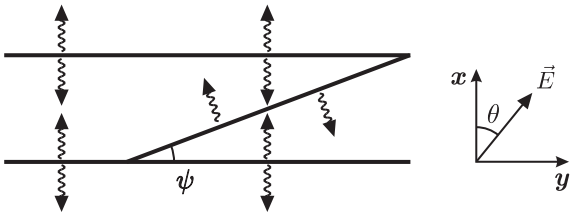

Figure 5.1. Composite slit structure consisting of a double slit, at left, and a three-slit section at right. The slanted slit is oriented at an angle ψ relative to the two parallel slits. When a light beam, polarized at an angle θ relative to the x direction, is incident on the structure, surface plasmons, indicated by wiggly arrows, are launched by each of the slits.

scattering channels is a scattering amplitude and phase. These corrugations can thus be seen as a multi-port splitter [24, 95]. Theoretically, this subject has been extensively researched by Maradudin and others [84, 94, 96–98].

Let us consider the case that a smooth and thin metal film is perforated by two close-lying long and narrow slits. Let us further assume that these two apertures are illuminated by a spatially coherent beam that is normally incident on the metal film. Each of the slits will give rise to both forward- and backward scattered light, and surface plasmons that run away from the apertures. Additionally, each aperture will scatter some of the surface-plasmon (SP) intensity that it receives from its partner into various output channels, namely a forward-scattered surface-plasmon, a backward-scattered SP, and scattered light, both towards the source and away from it. Consequently, interference will arise in all scattering channels. A signature of that interference is a modulation of the power measured in any of the output channels when the wavelength of the incident light is changed. By monitoring such modulation spectra one obtains information about the relative strengths of the interfering fields, i.e. of the transmission, reflection and scattering amplitudes and, in principle, also about their phase. While the amplitudes are easy to extract from the experimental data, the phase information often requires precise knowledge of the distance between the apertures that, in many cases, is not available with sufficient precision. Here we show that, by using a well-designed three-slit structure, the missing phase information can be obtained from a requirement of self-consistency, and is therefore available even when the distance between the various slits is not known with great accuracy.

5.2 Heuristic models

The system that we study here is depicted in Fig. 5.1. The left section forms a double-slit structure, in the section at right the twin slits are intersected by a slanted slit. All slits have a width $\approx \lambda/8$ so that a) their transmission is strongly polarized (see Chapter 6), b) they act as an effective source of surface plasmons for incident light that has a non-negligible polarization component perpendicular to the slit (TM-polarization) and c) their direct transmission is sufficiently small that the amplitudes of the directly transmitted light and the surface plasmon are of the same order of magnitude. In the experimental samples that we study, the double and triple slits are part of a single structure (see Fig. 5.2) so that the parallel slits in both structures are separated by the same distance d. In the case that we consider here the slit separation d is much smaller than the surface-plasmon amplitude damping length $L_{\mathrm{sp}} = 1/k''_{\mathrm{sp}} = 1/\mathrm{Im}(k_{\mathrm{sp}})$.

In the experiment we image the light that is transmitted by the slit structure. The signal that we then record on a specific pixel of our CCD-camera is directly proportional the power that is radiated by the corresponding point in the slit structure. Obviously, not all the radiated power is collected by our imaging lens (our source has a sub-wavelength extent in one transverse direction) but we can safely assume that the effect of this loss is equal for all source points. Consequently, we can simply model the measured signal at any point on the CCD as the square modulus of the local propagating field in the source, i.e., as the square modulus of the transmitted field.

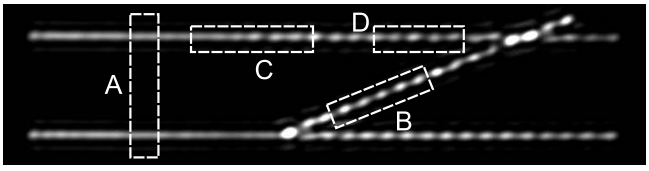

Figure 5.2. Image of one of the slit structures when illuminated by a plane wave at $\lambda = 742$ nm. The various sections that are indicated are discussed in the text.

We use area A to record the transmission of a double slit (see Section 5.2.1) in order to compare it, in Section 5.4.2, with the transmission of the slanted slit (area B, Section 5.2.2) in the three-slit system. Area C shows that the slanted slit acts as a line source of surface plasmons (see Section 5.4.4). By comparing the transmission of the slits in area A with the line-integrated transmission in area D we learn about the tunneling of surface plasmons across a nanoscale

slit. Finally, by analyzing the light transmitted in area D we show that, there, the polarization of the light is space variant.

5.2.1 Two-slit system

Let us first examine the two-slit part of our slit system (part A in Fig. 5.2). When illuminated by light that is polarized at an angle θ with respect to the x-axis, the transmitted field E_{slit} and detected signal S_{slit} can be written as (see Chapter 2, [61]):

$$E_{\text{slit}} \sim (1 + \alpha \exp[i(k_{\text{sp}} d + \phi_{\text{c}})]) \cos\theta, \tag{5.2}$$

$$S_{\text{slit}} \sim \left(1 + \alpha^2 + 2\alpha \cos[k_{\text{sp}} d + \phi_{\text{c}}]\right) \cos^2\theta, \tag{5.3}$$

where the factor 1 represents the light that is directly transmitted by the slit, $\alpha \exp(i\phi_{\text{c}})$ the light-SP-light coupling coefficient and k_{sp} the SP propagation constant (see Eq. (5.1)). Here we assume that the field directly transmitted by the slit and that which has been scattered into a plasmon, are reduced by the same factor $\cos\theta$ when the polarization of the incident light is changed. We further assume that we can disregard the effects due to the back-scattering of surface plasmons off the slits that are discussed in Chapter 4. Equation (5.3) predicts a sinusoidal modulation of the detected signal as a function of the surface-plasmon wave vector k_{sp} (see Chapter 2). Calculations based on rigorous diffraction theory suggest that $\phi_{\text{c}} = \pi$ [61, 90].

5.2.2 Three-slit system

The light emitted by the slanted slit in the three-slit system originates from three sources, namely, light that is directly transmitted by that slit, and two surface plasmons, launched by the two parallel slits. The amplitude of the field emitted by the slanted slit can therefore be written as:

$$E_{\text{slanted}} \sim \cos(\theta - \psi) + \left(\alpha' \exp[i(k_{\text{sp}} x + \phi_{\text{c}})] + \alpha' \exp[i(k_{\text{sp}}(d - x) + \phi_{\text{c}})]\right) \cos\theta, \tag{5.4}$$

so that the detected signal becomes

$$\begin{aligned} S_{\text{slanted}} \sim\ & \underbrace{\cos^2(\theta - \psi) + 2\alpha'^2 \cos^2\theta} \\ & + \underbrace{4\alpha' \cos(\theta - \psi) \cos\left[\frac{k_{\text{sp}} d}{2} + \phi_{\text{c}}\right] \cos\left[k_{\text{sp}}(x - \frac{d}{2})\right] \cos\theta} \\ & + \underbrace{2\alpha'^2 \cos\left[2k_{\text{sp}}(x - \frac{d}{2})\right] \cos^2\theta}\,. \end{aligned} \tag{5.5}$$

Again θ measures the angle between the polarization direction of the incident light and the x-axis, and $\alpha' = \alpha \cos\psi$. We assume that the amplitude for the scattering from a surface plasmon to a propagating light field by a slit is proportional to $\vec{k}_{\rm sp} \cdot \vec{n} = \cos\psi$ with $\vec{n}$ the in-plane normal to the slit. Here ψ is the angle subtended by the horizontal and slanted slits (see Fig. 5.1).

The terms contained in the first brace form a wavelength-independent background term; the term in the second brace (proportional to α') represents the interference between light directly transmitted by the slanted slit and the surface plasmons launched by the slits at the top and bottom, while the term in the third brace (proportional to α'^2) originates from the interference between the two counterpropagating plasmons launched by the top and bottom slits. The term due to the interference between transmitted light and surface plasmons has a spatial period equal to $\lambda_{\rm sp}$, while the plasmon-plasmon interference term has a spatial period of $\lambda_{\rm sp}/2$.

SP-SP interference

Because the plasmon strength is small ($\alpha \simeq 0.2$, see Chapter 4) the SP-SP interference, being proportional to α^2 will be difficult to observe. Fortunately, however, the term describing the light-SP interference can be made to vanish by tuning the wavelength of the incident light so that $\cos\left[k_{\rm sp} d/2 + \phi_{\rm c}\right] = 0$. At that wavelength it should be possible to observe the SP-SP interference, i.e., observe a surface-plasmon standing wave. One may argue that even under these circumstances it will be difficult to observe this high-spatial frequency intensity modulation, being at the limit of what can be observed using far-field techniques such as imaging. The trick lies in the fact that the slit is slanted so that the measured spatial pattern has a periodicity of $\lambda_{\rm sp}/(2\sin\psi)$, where ψ is the angle subtended by the parallel slits and the slanted slit.

At exactly this wavelength the signal coming from region A of our structure can be written as:

$$S_{\rm slit} \sim \left(1 + \alpha^2 - 2\alpha\cos\phi_{\rm c}\right)\cos^2\theta, \tag{5.6}$$

so that this signal is *minimal* when $\phi_{\rm c} = 0$, and *maximal* when $\phi_{\rm c} = \pi$. Obviously, the value of $\phi_{\rm c}$ is not limited to being an integer multiple of π; all values are, in principle, allowed.

Interestingly, we see that we have gained access to hitherto inaccessible information on the scattering phase $\phi_{\rm c}$ by a simple correlation measurement: the wavelength is tuned so that the light-SP interference in the slanted slit system vanishes and one observes the signal from the neighboring two-slit structure.

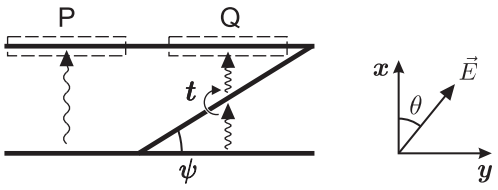

Figure 5.3. Setup for measuring the surface-plasmon tunneling amplitude t. Sections P and Q define the areas over which the signal should be integrated.

SP Tunneling

The images that we record also contain information on the *tunneling* of a surface plasmon across a slit, in our case the slanted slit. That information can be extracted by studying the signal, integrated along two sections of either the top or bottom slit (see Fig. 5.3), as a function of the wavelength of the incident light.

While the signal in section P is independent of the coordinate y, the signal in section Q is modulated due to the interference of the light transpiring through the top slit and the surface plasmon that is launched by the slanted slit (see Section 5.4.4). By integrating over a sufficiently large length of slit this interference pattern is washed out. Then we are no longer sensitive to the SP launched by the slanted slit. Alternatively, one can choose the polarization of the incident light to be parallel to the slanted slit ($\theta = \pi/2 - \psi$); in that case the slanted slit does not emit surface plasmons. The latter approach has a drawback in that the surface plasmons launched by the horizontal slits have a small amplitude (proportional to $\sin\psi$).

Assuming the incident light to be x-polarized, i.e., $\theta = 0$ we can write the y-averaged field amplitudes in sections P and Q as:

$$\overline{E}_{\mathrm{P}} \sim 1 + \alpha \exp[i(k_{\mathrm{sp}} d + \phi_{\mathrm{c}})], \tag{5.7}$$

$$\overline{E}_{\mathrm{Q}} \sim 1 + t\alpha \exp[i(k_{\mathrm{sp}} d + \phi_{\mathrm{c}} + \phi_{\mathrm{t}})], \tag{5.8}$$

where $\tilde{t} = t\exp(i\phi_{\mathrm{t}})$ is the surface-plasmon tunneling coefficient. The section-averaged signals can then be written as:

$$\overline{S}_{\mathrm{P}} \sim 1 + \alpha^2 + 2\alpha \cos[k_{\mathrm{sp}} d + \phi_{\mathrm{c}}], \tag{5.9}$$

$$\overline{S}_{\mathrm{Q}} \sim 1 + (t\alpha)^2 + 2t\alpha \cos[k_{\mathrm{sp}} d + \phi_{\mathrm{c}} + \phi_{\mathrm{t}}]. \tag{5.10}$$

When the signals are measured as a function of the wavelength of the incident light, the signal from both sections P and Q will vary sinusoidally

with a visibility equal to:

$$\mathcal{V}_{\mathrm{P}} = \frac{2\alpha}{1+\alpha^2} \simeq 2\alpha, \tag{5.11}$$

$$\mathcal{V}_{\mathrm{Q}} = \frac{2t\alpha}{1+(t\alpha)^2} \simeq 2t\alpha, \tag{5.12}$$

since $\alpha^2 \ll 1$. The ratio of the visibility of the spectrum in sections P and Q is a direct measure of the tunneling amplitude t. The value of the tunneling phase ϕ_{t} can be extracted from the shift in wavelength of the two spectra.

5.3 Experimental setup

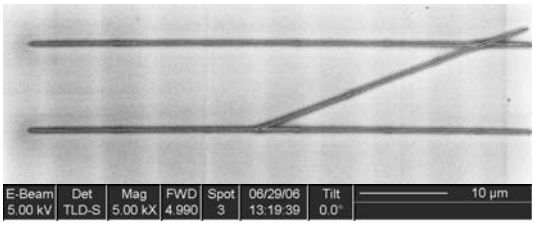

Figure 5.4. A SEM image of the sample.

Our sample consists of a 200 nm thick Au film sputtered on top of a ~ 10 nm thick Cr layer that adheres to a 0.5 mm thick glass substrate. Slits of 100 nm width are milled into this gold film with the help of a focussed-ion beam [52]. An image of a typical structure milled into the film, recorded with a scanning-electron microscope, is shown in Fig. 5.4. One sees two 60 μm long parallel slits, separated by a distance of 10 μm, and a third slit that intersects the other two at an angle of approximately 20°.

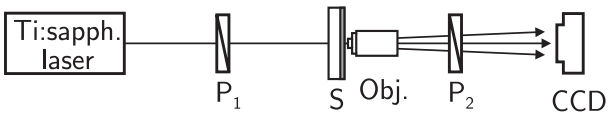

Figure 5.5. Experimental setup.

This structure is illuminated from the glass side by the unfocussed output beam of a Ti:Sapphire laser (Coherent, model 899), that is wavelength tunable

between 740 nm and 830 nm (see Fig. 5.5). The light that emerges from the metal nano-structure is collected by an oil-immersion microscope objective (100× magnification, 1.25 N.A.) and imaged on a CCD camera (Apogee, Alta U1). Due to the immersion oil on top of the gold film the surface-plasmon wavelength $\lambda_{\rm sp} = 2\pi/k_{\rm sp}$ at a particular frequency ω is much smaller than the free-space wavelength $2\pi c/\omega$, approximately being equal to $2\pi c/(n\omega)$, with n the oil's refractive index. Using the tabulated values of the complex refractive index of gold [53] ($\epsilon_{\rm Au} = -24.61 + 1.76i$ at $\lambda = 785$ nm) and the published value of the oil's refractive index ($n = 1.51$) we find $\lambda_{\rm sp} = 494$ nm when the wavelength of the incident light is 785 nm. The sample is surrounded by two polarizers; the one upstream from the sample allows us to choose the polarization of the incident light. The polarizer that is positioned downstream from the sample allows us to do an elementary polarization analysis of the light transmitted by the sample.

In the current experiment it is important that the slits are sufficiently narrow to be almost completely opaque for incident light that is TE-polarized, that is, polarized in a direction parallel to the slits. For that reason we favor 100 nm wide slits (see Chapter 6). Because of the peculiar shape of the milled structure (see Fig. 5.4) some part of the structure will transmit a non-negligible amount of light, whatever the (uniform) polarization of the incident light may be. Note that this also implies that surface plasmons will come into play for any input polarization.

5.4 Results and Discussion

Figure 5.6 shows a series of images of the three-slit part of our sample at incident wavelengths equal to, from top to bottom, $\lambda_{\rm inc} = 785$ nm, $\lambda_{\rm inc} = 805$ nm and $\lambda_{\rm inc} = 532$ nm, respectively. In all of these images the incident light is vertically polarized (see Fig. 5.1), i.e., perpendicular to the horizontal slits. One immediately notices the different modulation patterns in these three images, particularly along the slanted slit. The bottom image, obtained with incident light at a wavelength of 532 nm shows no modulation at all, simply as a consequence that surface plasmons on the gold-oil interface are very strongly damped at this wavelength ($\mathrm{Im}(k_{\rm sp}) = 1.7\ \mu\mathrm{m}^{-1}$ at $\lambda = 532$ nm). The other two images show quite similar patterns along the horizontal slits but different patterns along the slanted slit. We will discuss these differences in more detail below. Note that, in the image in the center ($\lambda_{\rm inc} = 785$ nm) we had to overexpose the horizontal slits in order to record the pattern along the slanted slit with sufficient signal to noise.

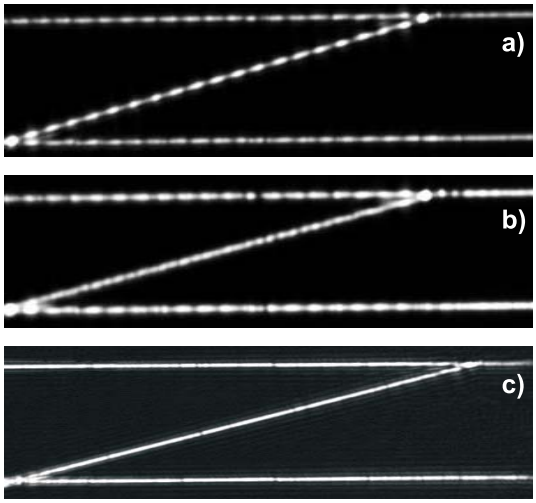

Figure 5.6. Images of the three-slit part of our slit system, obtained with vertically polarized incident light at $\lambda_{\rm inc} = 785$ nm (frame a); $\lambda_{\rm inc} = 805$ nm (frame b); $\lambda_{\rm inc} = 532$ nm (frame c). The center image is overexposed along the horizontal slits to bring out the weak modulation along the slanted slit with sufficient signal to noise.

5.4.1 Signal modulation along the slanted slit

A cross section of the measured signal along the slanted slit is shown in Fig. 5.7a and Fig. 5.7b for $\lambda_{\rm inc} = 785$ nm and $\lambda_{\rm inc} = 805$ nm, respectively. In frame a) we see a modulation pattern containing $\simeq 20$ maxima separated by ≈ 2.9 μm. Projected upon the x-axis we find a modulation period of ≈ 500 nm, which fits well with the calculated value (494 nm). A Fourier transform of the pattern along the slit (frame c) confirms that it is characterized by just one spatial frequency. The pattern arises because the surface plasmons, launched from the horizontal slits at the top and bottom are scattered by the slanted slit into transmitted light and interfere, at that slit, with the light that is directly transmitted by it. The pattern represents the term proportional to $\cos[k_{\rm sp}(x - d/2)]$ in Eq. (5.5). In a sense, the slanted slit, together with the light incident on it, provides us here with a tomographic cut through the surface-plasmon wave field at the gold-oil interface. Note, however, that we do not directly probe the field at the interface itself, but that we record the image of that field as generated by our optical setup, i.e., we pass through the far field. The field at the surface itself has recently been carefully studied using near-field techniques, in the context of a fiery debate on the nature of the surface wave [63, 99–103].

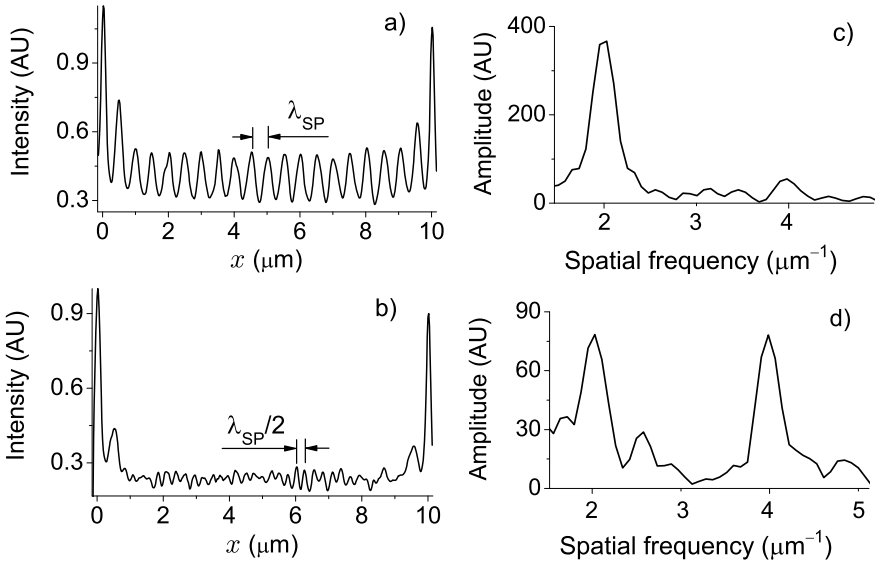

Figure 5.7. Cross-sections of the signal along the probe slit at $\lambda_{\mathrm{inc}} = 785$ (frame a) and 805 nm (frame b), respectively. Frames c) and d) show the corresponding spatial Fourier transforms of the signals along the slit.

For $\lambda_{\mathrm{inc}} = 805$ nm the visibility of the modulation pattern along the slanted slit (frame b) is much reduced. This pattern carries two modulation frequencies: $k_1/(2\pi) \approx 2\ \mu\mathrm{m}^{-1}$ and $k_2/(2\pi) \approx 4\ \mu\mathrm{m}^{-1}$, as shown in frame d). The low-frequency component of this spectrum has just been discussed and its presence is inadvertent. The high-frequency component comes about as a result of the interference of two counterpropagating surface plasmons between the slits; it corresponds to the last term in Eq. (5.5).

When the light incident on our multi-slit structure is vertically polarized, the pattern of Fig. 5.7b arises only at specific wavelengths, namely when $\cos(k_{\mathrm{sp}}d/2 + \phi_{\mathrm{c}}) = 0$. However, when the polarization of the incident light is chosen to be *parallel* to the slanted slit this pattern appears for *any* wavelength of the incident light for which surface plasmons are supported by the gold-oil interface and are not too heavily damped. At this polarization the slanted slit (being only 100 nm wide) does not directly transmit the incident light ($\cos(\theta - \psi) = 0$ in Eq. (5.5)) so that the SP-SP interference pattern corresponding to the term $\cos[2k_{\mathrm{sp}}(x - d/2)]$ in Eq. (5.5) can be observed.

Figures 5.7a and 5.7b show that, whatever the wavelength of the incident light, the signal rapidly rises near the end points of the slanted slit (at $x = 0\ \mu$m

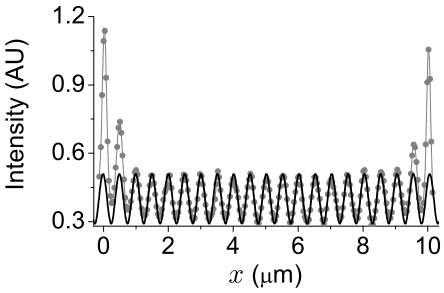

Figure 5.8. The data of Fig. 5.7a (grey curve) with a simple sinusoidal function (black curve) superposed. The excellent correspondence of the position of the maxima of the two curves indicates that our experimental data can be described by a single spatial frequency.

and $x = 10$ μm). There the slanted slit intersects one of the horizontal slits; we interpret the rapid rise of the signal along the slanted slit as being due to diffraction off the horizontal slits. Careful analysis of the full pattern of Fig. 5.7a shows that the modulation frequency of the pattern is constant along the full length of the slanted slit (see Fig. 5.8). Therefore, the rise of the signal near the horizontal slits does not herald the presence of an additional surface wave [51].

5.4.2 Coupling phase slip

In the two-step process, where incident light is first scattered at one slit into a surface plasmon which then is back-converted to light at the other slit, the total phase accrued can be written as [61]:

$$\Delta\Phi = k_{\mathrm{sp}} d + \phi_{\mathrm{c}}, \tag{5.13}$$

where d is the distance between the two slits and ϕ_{c} represents an additional phase slip. Numerical studies based on rigorous diffraction theory or a Green's function formalism predict that $\phi_{\mathrm{c}} = \pi$ [61, 90]; so far this theoretical prediction has not been verified in an experiment.

It would appear to be quite simple to experimentally verify this prediction, for instance by using the spectral modulation technique of Chapter 2. However, in order to find a reasonably exact value for ϕ_{c} the inaccuracy in $k_{\mathrm{sp}}d$ should be sufficiently small, but the slit separation d and the surface-plasmon wave vector k_{sp} are usually not precisely determined. The lack in precision in the experimental value of d (≈ 0.2 μm) stems from calibration inaccuracies

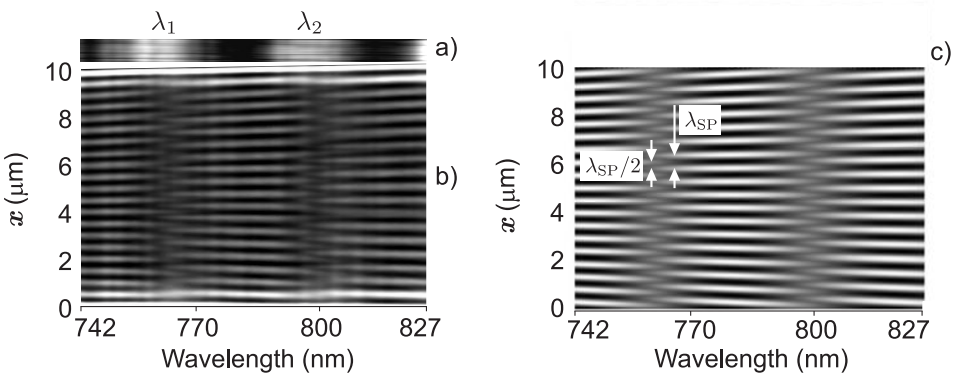

Figure 5.9. At left: Experimental data for the two-slit part of our sample (frame a) and the three-slit part (frame b), as a function of the wavelength of the incident radiation. The two-slit *maxima* occur at wavelengths $\lambda_1 = 760$ nm and $\lambda_2 = 796$ nm where the signal along the slanted slit shows a doubling of the spatial frequency. At right: calculated signal along the slanted slit according to Eq. (5.5) using $\phi_c = \pi$.

of the scanning-electron microscopes used by us, while the imprecision in k_{sp} stems from the fact that the dielectric coefficients of the gold film may not be equal to the published values [22, 53] and from the fact that Eq. (5.1) applies to an infinitely extending perfectly flat interface, which is not the case in the vicinity of our slits.

As discussed in section 5.2.2 our composite slit provides us with an opportunity to determine the phase slip ϕ_{c} without knowing the exact separation of the slits, by comparing the signal transmitted by the two-slit part with the pattern along the slanted slit in the three-slit part. The results of that experiment for the wavelength interval 742–827 nm are shown in the left frame of Fig. 5.9. The signal in the two-slit section (frame a) has maxima at $\lambda_{\mathrm{inc}} = 760$ nm and $\lambda_{\mathrm{inc}} = 796$ nm, exactly at those wavelengths where the signal along the slanted slit is rather low (frame b) and where it has twice the number of maxima as compared to the signal at other wavelengths. Frame c) displays the fringe structure along the slanted slit according to Eq (5.5) using $\phi_c = \pi$. The experimental and calculated fringe structures are in excellent agreement.

Whenever the signal in the two-slit section is maximum we have (see Eq. (5.3)):

$$k_{\mathrm{sp}} d + \phi_{\mathrm{c}} = 2\pi m, \tag{5.14}$$

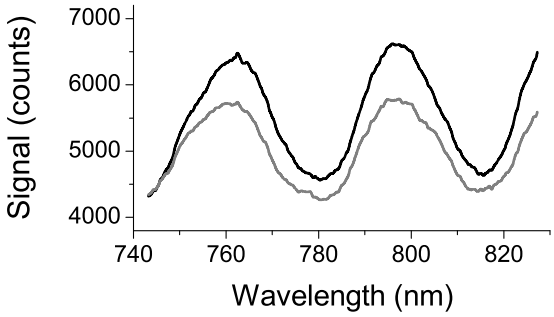

Figure 5.10. Transmission spectrum of the top slit of the two-slit section (black curve) and the top slit of the three-slit section (grey curve).

while the disappearance of the interference between the surface-plasmon and the incident light indicates that (see Eq. (5.5))

$$\frac{k_{\rm sp}d}{2} + \phi_{\rm c} = \pi/2 + 2\pi m'. \tag{5.15}$$

Here m and m' are integers. Together, these relations yield:

$$\phi_{\rm c} = \pi + 2\pi q, \tag{5.16}$$

where q is integer-valued.

5.4.3 Plasmon tunneling

As discussed in Section 5.2 the surface-plasmon tunneling amplitude and phase can also be extracted from a comparison of the signals transmitted by the two-slit and three-slit parts of our sample. However, we now focus on the spatial average of the signal along the horizontal slits in the two- and three-slit sections, respectively. The experimental results are shown in Fig. 5.10 where the black curve displays the results for the two-slit section (section P in Fig. 5.3) and the grey curve those for the three-slit part (section Q in Fig. 5.3). Form these spectra we derive values for the visibility: $\mathcal{V}_{\rm P} = 0.17$ and $\mathcal{V}_{\rm Q} = 0.14$. Using Eqns. (5.11) and (5.12) we find the tunneling amplitude $t \simeq 0.8$. By noting that the two spectra are well aligned we find that the tunneling phase shift $\phi_{\rm t} \approx 0$, in good agreement with the prediction of Janssen *et al.* [90].

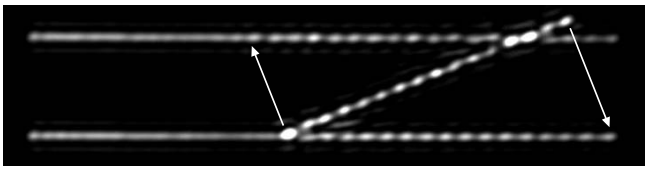

Figure 5.11. Transmitted-light image of a slightly different ion-beam milled sample exhibiting interference fringes in both the horizontal and slanted slits. The arrows indicate the propagation directions of the plane-wave surface plasmons emitted by the slanted slit.

5.4.4 Slanted slit as a source of surface plasmons

So far we have concentrated on the role of the slanted slit as a "probe" of the surface-plasmon field, generated by the two parallel slits. That, of course, is a simplification since the slanted slit will, in general, also emit surface plasmons. This is most easily seen by noting that the signal along the parallel slits is modulated in a manner similar to the signal along the slanted slit (see Fig. 5.11). One can easily show that the spatial frequency of the signal along the horizontal slit is equal to $k = k_{\mathrm{sp}} \sin\psi$, with ψ the angle subtended by the slanted and horizontal slits. The length of the interference pattern along the horizontal slits indicates that the surface plasmon launched by the slanted slit propagates as a plane wave along the interface.

This being said, one may ask whether the signal along the slanted slit may be affected by the surface plasmons emitted by this same slit after reflection from the two horizontal slits. For vertically polarized incident light one may argue that the amplitude of the light field transpiring through the slanted slit as a result of such a reflected plasmon is proportional to $\alpha|r|\cos\psi\sin 2\psi$, with $|r|^2$ the surface-plasmon reflection probability, which we have assumed to be independent of the angle of incidence (of the surface plasmon on a slit). For $\psi \approx 10^\circ$ as in the present experiment and $|r| \simeq \alpha$ (see Chapter 4) we get $\alpha|r|\cos\psi\sin 2\psi = 0.33\alpha^2$, a factor 6 smaller than the SP-SP interference effect discussed before. Therefore we can safely ignore these reflections.

If we choose the incident light to be y-polarized, the horizontal slits will transmit a very small fraction of the incident light although the frequency of the incident light is well beyond cut-off (slit width $\approx \lambda/8$, see Chapter 6). The surface plasmons, generated at the slanted slit (with low efficiency because the incident light is polarized almost parallel to this slit) will propagate towards the horizontal slits and will be partially scattered there into vertically polarized light. So the light emanating from the horizontal slits will have both vertically (due to SPs) and horizontally (due to tunneling) polarized components. The

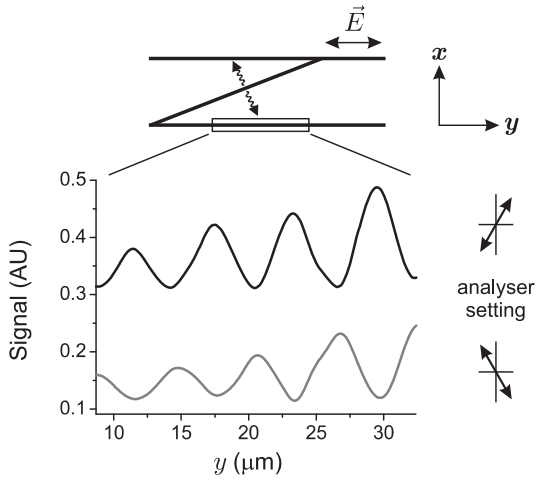

Figure 5.12. Experimental arrangement for observing a plasmon-induced space-variant polarization. The incident light is polarized parallel to the horizontal slits, which are sufficiently wide to be slightly transmitting. Surface plasmons launched by the slanted slit generate light at the horizontal slit that is vertically polarized. The two curves at the bottom show the space-dependent signal as transmitted by a uniform polarizer, for two settings of the polarizer transmission axis. The upper black curve is manually off-set from the grey curve for distinction.

phase difference between these components depends on the position along the horizontal slit because the vertically polarized component has its source in the slanted slit. We therefore expect the polarization to be space-variant along the horizontal slits.

We have studied this effect using a three-slit structure with somewhat wider slits (200 nm instead of 100 nm) and a more acute angle between the slanted and horizontal slits ($\approx 5°$ instead of $\approx 10°$). The results are shown in Fig. 5.12, where, in addition to a sketch of the slit structure, we show the spatial modulation of the signal along the bottom horizontal slit for two orientations of the analyzing polarizer that is positioned in front of our CCD-camera.

First, we note that the *amplitude* of the vertically and horizontally polarized components of the light coming out of the bottom slit should only weakly depend on the coordinate y. Their relative *phase*, however, will be a linear function of y, because of the angle subtended by the slanted and horizontal slits. Where the phase difference $\delta\phi = m\pi$, with m an integer, the output polarization will be linear. There are two sets of points where this is the case:

those where m is even (the vertically and horizontally polarized components are in phase) and those with m odd, where the vertically and horizontally polarized components are π out of phase. We can now orient the analyzing polarizer so that it extinguishes the light coming from those points where m is even, or those where m is odd. When the analyzer is oriented so that the even m points are extinguished, the points where m is odd will be bright, and when the analyzer is oriented so that the m is odd points are extinguished, the even m points will be bright. Both cases are shown in Fig. 5.12. In this experiment the polarization of the incident light is chosen so that the space-variant effect is most easily observed. In our configuration with differently oriented slits this effect occurs for any polarization of the incident light, but it may be difficult to observe in the most general case.

5.5 Conclusions

By using simple two- and three-slit structures milled in a gold metal film we have been able to directly measure the phase associated with the double-scattering process where incident light is converted into a surface plasmon in a sub-wavelength slit and back-converted to light in a neighboring slit. We have found this phase to be $\pi \pm 5\%$, in good agreement with predictions based on rigorous diffraction theory.

These structures also allow us to measure the amplitude and phase of the process where a surface plasmon tunnels across a sub-wavelength slit in a gold metal film. Finally, we have shown that the polarization of the light transmitted by such a structure can be space variant.

5.6 Appendix: Towards a complete picture of surface-plasmon scattering (unpublished)

The scattering of light and surface plasmons at a sub-wavelength slit is one of the central issues discussed in this thesis. By using various experimental techniques we have determined the scattering phase of the process (see Fig. 5.13)

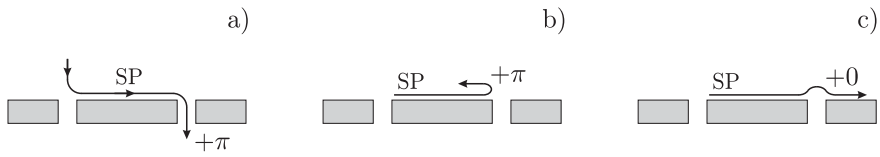

Figure 5.13. Scattering processes of light and surface plasmons.

a) where a wave incident from free space scatters into a surface plasmon and re-scatters into a propagating mode of the slit; this phase is equal to π (mod. 2π).

b) where a surface plasmon, incident on such a slit is back-scattered into a surface plasmon; this phase is equal to π (mod. 2π).

c) where a surface plasmon "jumps over" a slit; this phase is equal to 0 (mod. 2π).

The wavelengths where constructive or destructive interference occurs in the various scattering channels are determined by these phase factors, in addition to the propagation phase $k'd$ (with k' the real part of the surface-plasmon wave vector k_{sp} and d the distance between the slits).

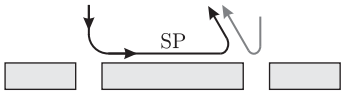

Figure 5.14. One-step and two-step scattering processes that give rise to interference in back-scattering. The two-step process has a surface plasmon as an intermediate state.

So far, we have neglected one important scattering process and thus one additional channel where interference can occur. This channel regards the *direct back-scattering of light off the slit*. The so scattered light interferes with light that originates at the other slit, is scattered into a plasmon, and is re-scattered into light (see Fig. 5.14).

A priori, it is not known how the interference in the back-scattered light relates to that in the transmitted channel, that is, whether the interference features in transmission and back-scattering are in phase, π out of phase, or something else. Figure 5.15 shows the result of an experiment. The back-scattered light is collected over a wide range of back-scatter angles; it does not contain the light that is directly reflected by the metal.

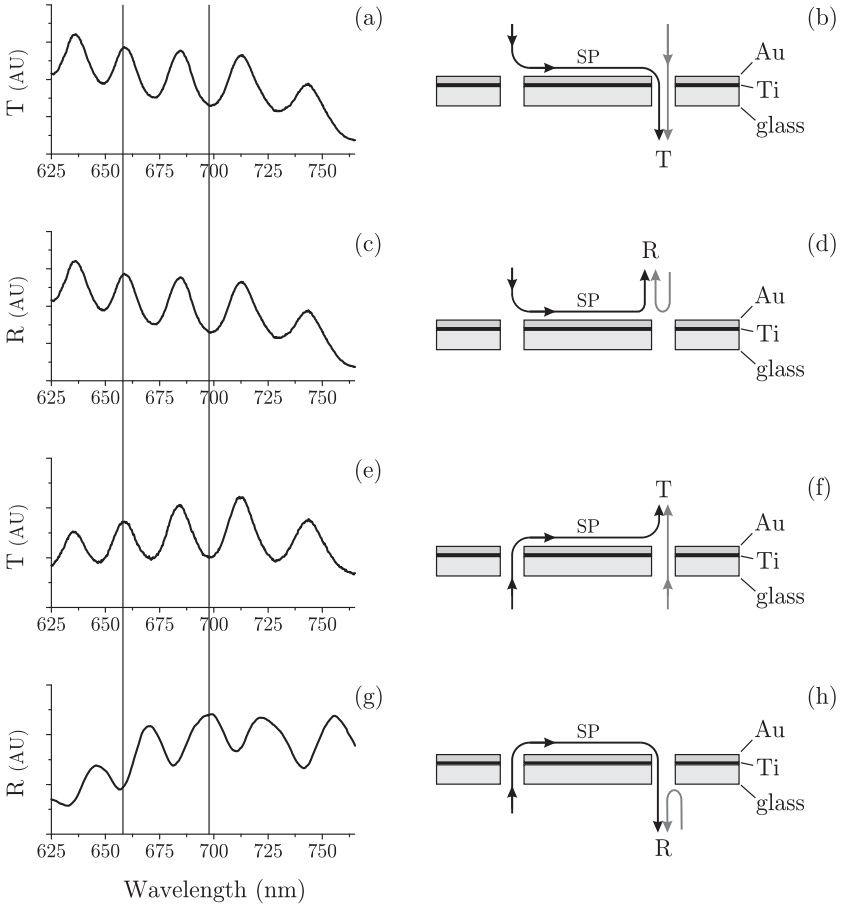

Figure 5.15. Spectra of transmitted light (a and e) and back-scattered light (c and g), with light incident on the metallic side of the sample (a and c), and on the glass side of the sample (e and g). For each of the spectra on the left, the diagrams on the right indicate the paths that interfere. Note the stacking of the materials in the sample; the 10 nm thin titanium layer between the gold and the glass serves two purposes. It acts as an adhesion layer for the gold and serves to rapidly damp the surface plasmons that are launched at the glass/gold interface.

Evidently, when the light is incident on the metallic side of the sample, the transmission and "reflection" spectra are very similar. However, when the light is incident on the glass side of the sample the transmission and "reflection" spectra have a phase difference that varies somewhat with wavelength, being $\approx \pi$. Note, that the experimental results show that the "reflection" spectra depend on the orientation of the sample, i.e, the side of the sample that is turned towards the light source matters. Violation of reciprocity is not at stake here because the system is not loss-free.

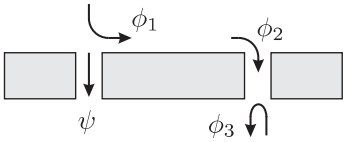

Figure 5.16. Nontrivial phase shifts for various scattering processes at sub-wavelength slits in thin metal films.

The collected experimental results induce us to present a heuristic model of the scattering of light and surface plasmons at sub-wavelength slits (see Fig. 5.16). This model is based on the following assumptions:

- A nontrivial phase shift of ϕ_1 is associated with the process where light, incident from free space, is scattered into a surface plasmon. The same phase shift occurs when a surface plasmon is scattered into free space.
- A nontrivial phase shift of ϕ_2 is associated with the process where light, propagating as a slit mode, scatters into a surface plasmon. The identical phase shift occurs when a surface plasmon is scattered into a slit mode.
- When a free-space mode is incident on a slit and is back-scattered, it accrues a nontrivial phase shift due to Fresnel reflection equal to ϕ_3, with $|\phi_3| = \pi$.
- When light propagates as a slit mode it acquires a phase $\psi = k_0\, n_z\, t$. Here t is the film thickness (the length of the waveguide), n_z the effective mode index, and $k_0 = \omega/c$ the free-space wave vector of the incident light. For the sample under investigation (see Chapter 6) we have $\psi \simeq \pi/2$.

We can now associate the following phase differences with the interfering paths in Fig. 5.15. From previous measurements (Chapter 5) we know that $\phi_1 + \phi_2 = \pi$ and that $\phi_3 = \pi$. The experiment of Fig. 5.15 shows that $\Delta\Phi_1 = \Delta\Phi_2$ so that

$$|\phi_1 - \phi_2| = |\phi_3| = \pi. \tag{5.17}$$

Pathway	Frame	Relative phase
Transmission	b, f	$\Delta\Phi_1 = k'd + \phi_1 + \phi_2$
Reflection in air	d	$\Delta\Phi_2 = k'd + 2\phi_1 - \phi_3$
Reflection in glass	h	$\Delta\Phi_3 = k'd + 2\phi_2 - \phi_3 + 2\psi$

Table 5.1. Phase differences for various interfering pathways in Fig. 5.15.

From the "reflection in glass" spectrum we deduce that

$$|2\phi_2 - \phi_3| = \pi. \tag{5.18}$$

Since $|\phi_3| = \pi$ we have $|\phi_2| = \pi$ or $\phi_2 = 0$, all modulo 2π. Combining with Eq. (5.17) yields the following combinations:

$$|\phi_1| = \pi \quad |\phi_2| = 0 \quad |\phi_3| = \pi, \tag{5.19}$$

$$|\phi_1| = 0 \quad |\phi_2| = \pi \quad |\phi_3| = \pi. \tag{5.20}$$

The first solution is in agreement with the prediction of Ref. [90], the other not.